Tuning the Spin Transition and Carrier Type in Rare-Earth Cobaltates via Compositional Complexity

*Alan Zhang[1], Sangheon Oh[1], Byoung Ki Choi[2,3], Eli Rotenberg[3], Timothy D. Brown[1] Catalin D. Spataru[1], Eli Kinigstein[3], Jinghua Guo[3], Joshua D. Sugar[1], Elena Salagre[1], Arantzazu Mascaraque[4], Enrique G. Michel[5,6], Alison C. Shad[1], Jacklyn Zhu[1] Matthew D. Witman[1], Suhas Kumar[1], A. Alec Talin[1] and Elliot J. Fuller[1]**

[1]Sandia National Laboratories, 7011 East Ave. Livermore, CA 94550, United States of America

[2]Department of Electrical and Computer Engineering, Texas A&M University, College Station, TX 3127, United States of America

[3]Advanced Light Source, Lawrence Berkeley National Laboratory, Berkeley, California 94720, United States of America

[4] Departamento de Física de Materiales, Universidad Complutense de Madrid, 28040 Madrid, Spain

[5]Departamento de Física de la Materia Condensada and Instituto Universitario de Ciencia de Materiales Nicolás Cabrera (INC), Universidad Autónoma de Madrid, 28049 Madrid, Spain

[6] IFIMAC (Condensed Matter Physics Center), Universidad Autónoma de Madrid, 28049 Madrid, Spain

ABSTRACT

There is growing interest in material candidates with properties that can be engineered beyond traditional design limits. Compositionally complex oxides, often called high entropy oxides, are excellent candidates, wherein a lattice site shares more than four cations, forming single-phase solid solutions with unique properties. However, the nature of compositional complexity in dictating properties remains unclear, with characteristics that are difficult to calculate from first principles. Here, we demonstrate compositional complexity as a tunable parameter in a spin-transition oxide semiconductor $La_{1-x}(Nd, Sm, Gd, Y)_{x/4}CoO_3$, by varying the population x of rare

earth cations over $0.00 \leq x \leq 0.80$. Across the series, increasing complexity is revealed to systematically improve crystallinity, increase the amount of electron versus hole carriers, and tune the spin transition temperature and on-off ratio. At high a population (x=0.8), Seebeck measurements indicate a crossover from hole-majority to electron-majority conduction without the introduction of conventional electron donors, and we propose tunable complexity as new method to dope semiconductors. First principles calculations combined with angle resolved photoemission reveal an unconventional doping mechanism of lattice distortions leading to asymmetric hole localization over electrons. Thus, we demonstrate that tunable complexity is a facile knob to improve crystallinity, tune electronic transitions, and to dope semiconductors beyond traditional means.

KEYWORDS

oxide, high entropy, cobaltate, spin transition

INTRODUCTION

Disorder can have strong effect on material properties, and in some cases, enhance performance or increase functionality. Compositionally complex materials, typically called high entropy materials, have received a surge of interest due to compositional site-disorder leading to intriguing performance enhancements in a wide range of areas, including thermoelectric devices[1], catalysts[2] and thermal barriers[3]. In particular, compositionally complex oxides (CCO)[4] are of interest due to enhanced performance and function as electronic and energy materials, with applications in computer memory[5], capacitors[6] and electrocatalysts[7], among others. However, despite their intriguing behavior, a fundamental understanding of complexity and entropy in CCO remains elusive. For example, the definition of what constitutes a “high-entropy”

material is under debate[8, 9], and it is unclear how complexity manifests magnetic order[10, 11] or new correlated phases or transitions[12]. Therefore, work must be done to unravel the effects of complexity and entropy versus simple alloying effects, and new descriptors and/or rules must be developed to enable rational design of CCO with enhanced performance or new functionality. In that vein, an unexplored line of investigation is the study of complexity itself as a tunable parameter for CCO systems. Such a study offers two exciting opportunities: first, tunable complexity can reveal new functionalities that have been overlooked due to a focus on compositional ratios in CCOs. Second, the nature of complexity and its role in determining functional properties can be revealed through systematic investigation.

To address these scientific challenges and to discover new functionality in CCOs, we introduce compositional complexity to a well-studied oxide semiconductor, $LaCoO_3$. In the $LaCoO_3$ perovskite structure, the interplay between spin and lattice degrees of freedom leads to a spin transition at 90 K and a broad semiconductor-to-metal transition (SMT) between 300 K and 600 K (Figure 1a). For $LaCoO_3$, the spin pairing energy P competes with the energy gap Δ between e_g and t_{2g} states in the octahedral field splitting. A low-spin (LS) configuration $\left[t_{2g}^6, S = 0\right]$ is promoted to a high-spin (HS) configuration $\left[t_{2g}^4 e_g^2, S = 2\right]$ as temperature is increased[13]. Controversy remains over the existence of an intermediate spin (IS) state. However, recent theoretical and experimental work found that that the spin transition at 90 K is from LS to an IS configuration $\left[t_{2g}^5, e_g^1\ S = 1\right]$, and the gradual SMT (occurring over 300-600 K) is concomitant with a subsequent spin transition to the HS state. Despite this controversy, as lanthanum is substituted for rare-earths with smaller radii, a well-characterized and systematic increase in the SMT transition temperature is observed due to a decrease in the Co-O-Co bond angle[14]. Additionally, the rare-earth cobaltates exhibit p-type semiconducting behavior (at 300K) with a

systematic increase in the gap with smaller radii of the rare-earths. Thus, the rare earth cobaltates present an ideal system to investigate the effects of complexity because of two reasons: (1) compositional complexity at the rare-earth site has the potential to become a tunable parameter without requiring entropy stabilization for phase purity, and (2) the effects of complexity can be isolated by comparing with the properties of well-understood ternary compounds or 'simple alloying behavior'.

RESULTS

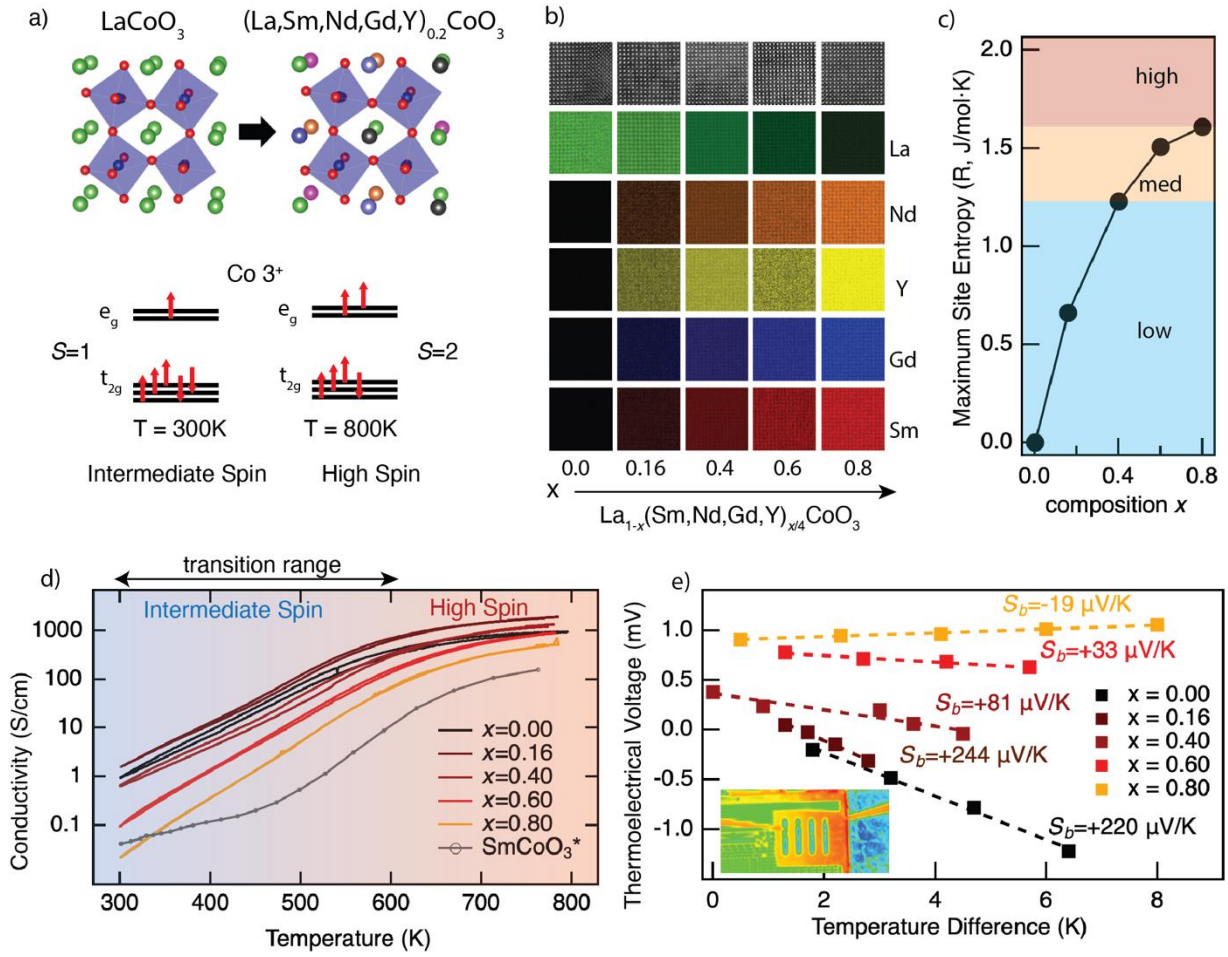

Figure 1. Compositionally complex rare-earth cobaltates. (a) $LaCoO_3$ perovskite structure (left), a compositionally complex version with multiple rare earth cations (right), and corresponding spin configuration diagrams (bottom). (b) HRTEM cross sections of epitaxial thin films across the composition series from x=0.00-0.80, with corresponding mapping of the constituent metal elements obtained using EDS. Each image has a lateral dimension of 6.4 nm. (c) Maximal site configurational entropy plotted as a function of composition. (d) Conductivity versus temperature at varying compositions (e) Room-temperature measurements of the thermoelectric voltage as a function of composition with fits indicating the Seebeck coefficient. The inset is an infrared image of thermal gradients taken during measurements.

To systematically tune complexity and entropy, we synthesize epitaxial films of $La_{1-x}(Nd, Sm, Gd, Y)_{x/4}CoO_3$ with compositions that span from x = 0.00 to x = 0.80 (Figure 1a). All compositions are synthesized by pulsed laser deposition (PLD) on $LaAlO_3$ single crystal substrates at T = 923K and an oxygen pressure of 100 mTorr. To create intermediate compositions in the range of x = 0.00-0.80, we vary the duty cycle between a target of x = 0.00 and x = 0.80 composition with sub-monolayer shot counts between cycles (by fixing the total deposition thickness of 68 nm). Following deposition, all films are annealed at T = 800K in air to eliminate any potential effects of oxygen vacancies created during growth (detailed in the methods section). The $La_{1-x}(Nd, Sm, Gd, Y)_{x/4}CoO_3$ series exhibits a systematic increase in the population of complex cations with x which spans three critical 'regimes' (Figure 1c) quantified by maximal site-configurational entropy (low, medium and high) and as proposed by previous theoretical work[8]. For example, compounds with high-configurational site entropy (as with x=0.80) have been proposed to benefit from entropy stabilization effects leading to reduced secondary phases and defects, among other effects. A combination of x-ray diffraction and high-resolution transmission electron microscopy (HRTEM) are used to determine that all samples were perovskite phase with a systematic decrease in the c-axis as expected for progressively smaller average rare-earth radii. The EDS maps are labeled with the assumed composition from the duty cycling between the end member targets. The maps were used to determine that the compositions between x = 0.00 to x = 0.80 were as expected from duty cycling within the error of the EDS technique (a few percent). Figure 1b displays HRTEM cross sections for films with varying compositions in the range $0.00 \leq x \leq 0.80$, along with mapping of the elemental compositions using energy dispersive x-ray spectroscopy (EDS). The high-resolution compositional maps reinforce

the spatially uniform nature of the elemental distribution at the atomic scale. Additional HRTEM can be found in the supplementary text (Figure S2).

The electronic conductivity (σ) plotted against temperature (Figure 1d) reveal a combination of simple alloying effects and those we ascribe to compositional complexity. First, $LaCoO_3$ ($x = 0.00$, black) has a broad SMT transition from σ = 1 S/cm to σ =1,000 S/cm in the range of 300-800 K, similar to other reports of single crystals and high-quality epitaxial films[14]. At the most dilute compositional complexity of $x = 0.16$, we observe an increase in overall conductivity by a factor of two. As the composition varies from $x = 0.16$ to $x = 0.80$, a family of curves (dark brown to orange) with increasing ratio of conductivities obtained at the extreme temperatures ($\sigma_{T=800\ \mathrm{K}}/\sigma_{T=300\ \mathrm{K}}$) and decreasing conductivity at room temperature are both observed. Minor rate-dependent hysteresis loops are observed which are likely due to kinetically limited oxygen activity at the sample surface combined with the surface sensitive nature of thin film transport relative to bulk. Interestingly, the hysteresis loops are reduced with compositional complexity, likely due to slower kinetics for the CCOs. The transport curves demonstrate that tuning the population of complex cations can be used to systematically modulate the SMT transition threshold. For example, the temperature threshold required to reach 10 μS is shifted by 130 K across the series of different compositions. We anticipate such tunability to be immediately useful for engineering electronic devices that rely upon electrothermal thresholding, such as selectors[15], electrostatic discharge protectors[16] or radio frequency varistors[17] but with enhanced structural perfection (which we will discuss in detail later on) potentially leading to greater endurance.

While tunable thresholding is interesting from a technological perspective, and is consistent with a variation in the average rare-earth radius[14], the transport behavior in Figure 1c exhibits

significant deviations from what is expected from simple alloys. For ABO_3 perovskites, the factor $t \equiv (r_{AR} + r_O)/\sqrt{2}(r_B + r_O)$, where r_{AR} is the ionic radius of the A-site element, r_O is the ionic radius of oxygen, and r_B is the ionic radius of the B-site element, is predictive of transition temperatures in cobaltates, nickelates and their simple alloys (e.g. $Nd_{0.5}Sm_{0.5}NiO_3$)[14, 18]. Using a composition-weighted average across rare-earth radii, $r_A \equiv \bar{r}_A = \sum_{i \in A} x_i r_i$ (A is the set of all A-site elements, x_i are the A-site fractions, and r_i their ionic radii) for composition x = 0.8, we calculate t = 0.962, the transport characteristics of which should be closest to that of $SmCoO_3$ with t = 0.958[19]. However, transport measurements of $SmCoO_3$ by Scherrer et. al. (Figure 1c grey, circles) reveals an on-off ratio ($\sigma_{T=800\ K}/\sigma_{T=300\ K}$) that is lower than our measurements by a factor of 6 [20]. Furthermore, compared to Scherrer et al., in our measurements, the curve at x = 0.80 is shifted by 80 K higher in temperature (to reach 10 μS), and there is a large difference in slope at lower temperatures (close to 300 K). The larger on-off ratio of the CCO for a given temperature threshold is useful from a technological perspective (i.e., a larger magnitude switching at lower temperatures). However, such differences also point to novel electronic phases. For example, Mazza et al. demonstrated that new electronic phases were responsible for a 60 K shift in the insulator-metal transition temperature of nickelate CCO[12].

As further evidence of novel electronic properties, measurements of Seebeck coefficient (S_b) collected at room temperature (Figure 1d) reveal a systematic change from majority hole to electron carriers as complexity increases. For x = 0.00 and x = 0.16, we observe similar p-type behavior with a Seebeck coefficient of S_b = +220 μV/K and +244 μV/K, respectively. However, at x = 0.40 and x = 0.60, S_b drops to +81.3 μV/K and +32.0 μV/K, respectively. At x = 0.80 we observe a cross-over to majority n-type behavior with S_b = -19.3 μV/K. The carrier type crossover is notable, because (1) it is not observed in simple rare-earth cobaltate alloys without dopants, (2)

other studies of high entropy cobaltates have not shown this previously, and (3) it has potential to open a new avenue for engineering carrier type beyond traditional doping methods through tuning populations of complex cations at specific lattice sites.

Point (1) suggests that compositional complexity is responsible for the crossover in the majority carrier type of the system. The rare earths in our compounds are all in oxidation state of 3+ and thus do not act as acceptors or donors. Furthermore, without traditional doping methods (i.e., substitutions with different oxidation states), all compositionally simple compounds ($LaCoO_3$, $SmCoO_3$, etc.) are p-type conductors. Thus, this shift in the carrier type for x = 0.8 suggests substantial deviation from basic alloying effects. Next, we address point (2): previous work by Kumar *et. al.* investigated the thermoelectric properties of a similarly complex alloy $(\mathrm{LaNdPrSmEu})_{1-x}\mathrm{Sr}_x\mathrm{CoO}_3$ and found conventional majority hole-type conduction for all values x[21]. Therefore, design rules to determine when carrier crossover occurs in complex materials are needed, and we propose such rules later on. We address point (3) by noting that tuning carrier type with complexity could be potentially extended more generally to other systems that might benefit from structural enhancements due to entropy stabilization and/or where charge donors have reached their limits of doping or introduce other undesired effects. Finally, we note that a previous works studied transport in bulk powders of $\mathrm{La}_{0.2}(\mathrm{Nd,Sm,Gd,Y})_{0.2}\mathrm{CoO}_3$, but either did not investigate carrier type[22] or did not investigate the high-temperature spin transition[23].

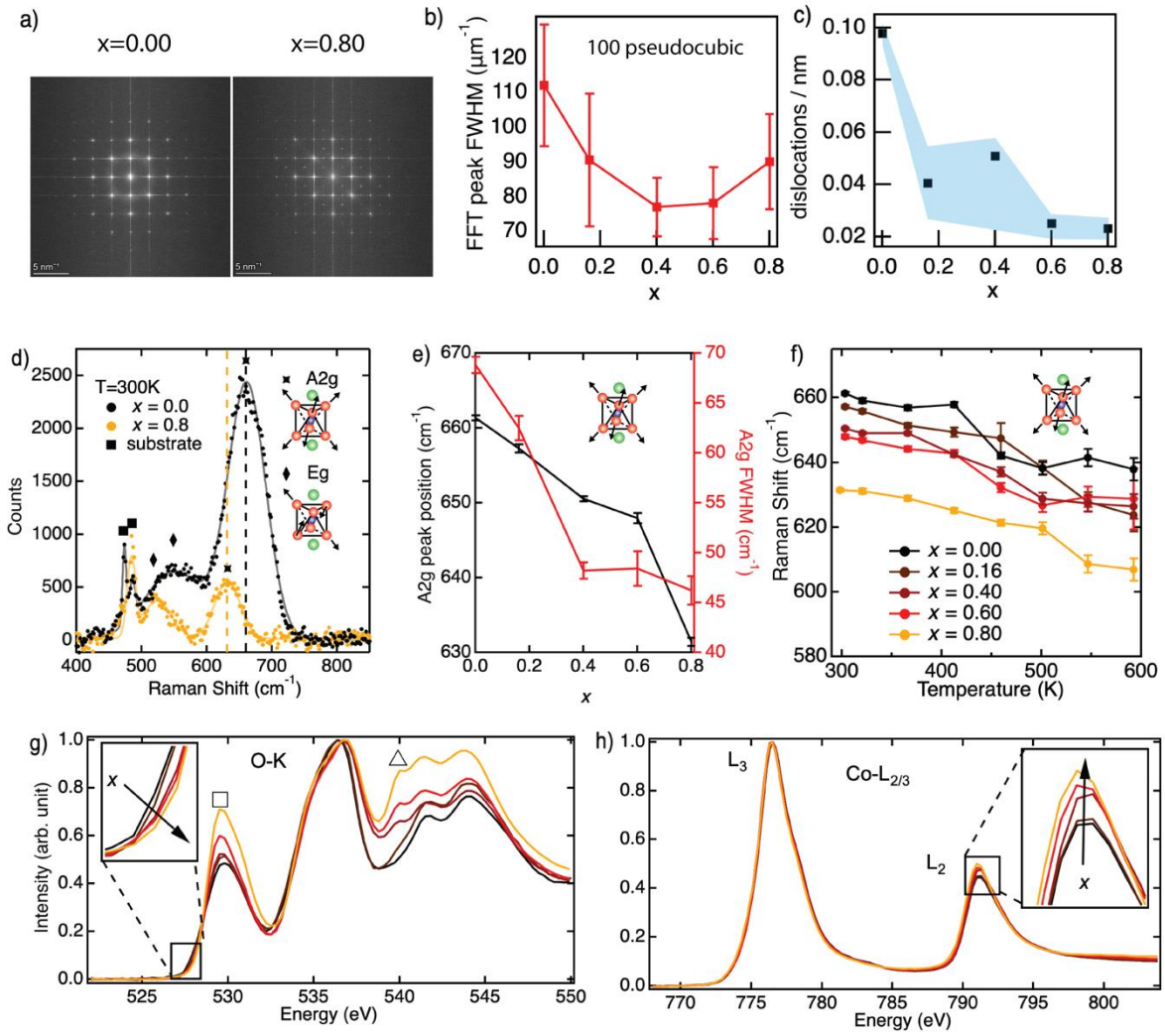

Figure 2. HRTEM, Raman and X-ray absorption spectroscopy of compositionally complex perovskite cobaltate alloys. (a) Fourier transform (FT) of HRTEM images of $x = 0.00$ and $x = 0.80$. Additional peaks associated with orthorhombic distortion were observed in $x = 0.80$ (b) The full width at half maximum (FWHM) of the FT peak associated with the 100 pseudocubic reflection plotted as a function of composition x (c) Dislocations found in HRTEM images as a function of composition. The average value is plotted in black width shaded blue indicating the range. (d) Raman spectra of breathing (A2g) and quadrupole (Eg) modes for compositions $x = 0.00$ (black) and $x = 0.80$ (orange) obtained at room temperature (dots) with multi-peak fits to the spectra

(solid). Inset diagram illustrates the motion of oxygen atoms associated with each mode. (e) Breathing mode shift as a function of composition x plotted along the FWHM. (f) Breathing mode shift as a function of temperature for all compositions x = 0.00-0.80. The X-ray absorption spectra of the O K and Co L-edges are displayed in (g) and (h), respectively. The inset in (g) displays spectral loss from the shoulder of the low energy 530 eV peak indicated by a square. A triangle indicates the location of new peaks, which appear and grow with composition x. (h) The inset shows an increase in spectral weight of the Co-L_2 edge with composition x.

To determine how structure and distortions play a role in the electronic properties we carried out more detailed HRTEM analysis. Figure 2a displays Fourier transforms of real space images corresponding to x = 0.00 and x = 0.80. Sharp peaks are observed with positions indicating the pseudocubic structure. As expected from decreasing rare earth radii, the series exhibits a shift from rhombohedral to orthorhombic distortion (seen as additional peaks in Figure 2a, right panel) with the crossover occurring at x = 0.40. In Fig. 2b, the FFT peak width is plotted as a function of composition. We additionally carried out a geometric phase analysis (GPA) to quantify the strain occurring in the samples which can be found in the supplementary text Figure S3. We identify three critical phenomena contributing to 'crystallinity' as quantified by the widths in the Fourier transform peaks and the GPA histogram widths. First, better lattice matching will reduce variations in the lattice parameter over the thickness of the film due to strain relief which will decrease widths. Second, defects such as dislocations will increase widths due to a disruption of the lattice and local strain fields. And finally, correlated atomic site structural distortions due to varying rare earth radii may again broaden the widths.

We discuss the trends in the FFT and GPA analysis within the context of the mechanisms described above. First, in Figure 2b, an interesting trend is observed in the Fourier transform peak width as

a function of composition, where improvements to crystallinity (narrower widths) are found as soon as $x = 0.16$. While GPA analysis suggests strain is also reduced due to better lattice matching from $x = 0.00$ though $x = 0.60$, the strain tensor histograms ϵ_{xx}, ϵ_{yy} for both $x = 0.00$ and $x = 0.16$ are nearly matched in overall strain compared with the rest of the composition series (see Fig. S3), but the ϵ_{yy} histogram width and the FFT widths are substantially sharpened indicating that another mechanism may be at play such as defect density. We studied dislocation defects observed in the films. In Fig 2c, a notable drop in dislocation density is observed from $x = 0.00$ to $x = 0.16$, from 0.10 dislocations/nm to 0.04 dislocations/nm, respectively, after which dislocation density saturates. An open question is: At what level of complexity can stabilization due to configurational entropy be used to suppress defect formation, for example, suppressing misfit dislocations? Reducing defect densities and improving crystallinity is a tantalizing prospect for improving materials (e.g., reducing carrier recombination rates in semiconductors), especially if defects could be reduced by dilute molar fractions of additional cations (i.e. at $x = 0.16$). We suspect the reduction in defect densities are responsible for the increase in electrical conductivity of the films (by a factor of 2) at $x = 0.16$ due to lowered electronic scattering (Figure 1d).

While the sudden drop in dislocations and decrease in FFT peak and GPA histogram widths is intriguing, it was not possible to completely disentangle the effects of entropy stabilization versus lowered misfit strain with increasing x (see Figure S1, S2). Future work, ideally over a larger range of misfit strain, will be needed to determine precisely when entropy stabilization effects win out over enthalpic driving forces yielding lower defect densities. At larger fractions of $x = 0.40$, the improvements saturate and at $x = 0.8$ the FFT peak and GPA histogram width ϵ_{yy} increases, signifying lower crystallinity, but with nearly the same dislocation density. While some of the effect may be due to the introduction of small tensile strain from $x = 0.6$ to $x = 0.8$, we hypothesize

that as x exceeds a threshold (of about 0.40), a competing effect from the growing structural distortions due to larger populations of Y atoms may be responsible for the trend in widths. Indeed, Y has a significantly smaller atomic radius than the lanthanides in our compounds and has been demonstrated to be responsible for distortions leading to non-trivial electronic structure previously[12]. Additionally, previous work has utilized GPA analysis to determine the variance in bond angles due to complexity at varying transition metal sites[24] which would contribute to FFT and GPA peak widths. However, for our compounds, the overall variance in radii is smaller and it is more challenging to quantify these angular distributions directly due to averaging through the sample lamella. Therefore, for a complete analysis we have focused on Raman spectroscopy which is less sensitive long-range disorder and more sensitive to atomic range effects.

Figure 2d is a plot of the Raman spectra of the quadrupole (Eg) and breathing (A2g) modes for compositions of x = 0.00 and x = 0.80 at T = 300K. While the symmetry reduction from $R\bar{3}c$ rhombohedral to *Pbnm* orthorhombic increases the number of active modes, we note the Eg and A2g modes is retained between the structures[25]. The intensity of the modes is reduced with complexity, and as expected, they are softened with composition due to higher-weight lanthanides. Despite a reduction in Raman intensity, the peaks widths are sharpened with increasing x, which we attribute to higher crystallinity (Figure 2e, red), with improvements occurring in the range x = 0.16-0.40, corroborated by the HRTEM data (Figure 2b). Similar to FFT and GPA trends, the breathing FWHM yields no improvement (within error) past x=0.40 despite better lattice matching at x = 0.6, indicating a possible competing effect from higher populations of Y atoms causing greater atomic range structural distortions. Additionally, Raman spectroscopy informs about the structural component of the SMT. The SMT in $LaCoO_3$ is accompanied by Jahn-Teller (JT) distortions, which have been shown to soften the breathing (A2g) mode at temperature[26]. Raman

spectroscopy in the range x = 0.00-0.80 as a function of temperature in the range T = 300-600K are plotted in Figure 2f. Here, we observe a systematic shift in the breathing mode of roughly 20 cm^{-1} over a temperature change of $\Delta T = 300$ K for all compositions. The softening between compositions is roughly maintained over the temperature range, although with increased uncertainty in the fitting and a larger scatter in the data at higher temperatures. Interestingly, each composition is clearly undergoing similar JT distortions through the SMT."

Next, we discuss X-ray absorption spectroscopy (XAS) performed on the series of compositions, which supports conclusions from electronic transport but that also points to new electronic hybridizations, likely due to atomic-site structural distortions. The sample drain current and X-ray fluorescence intensity are measured as a function of X-ray energy (normal incidence) and used to construct the Total Electron Yield (TEY). More details can be found the methods section. Figure 2g,h are of the O-K edge and Co-L edge TEY XAS, respectively. Three critical features are observed in the O-K edge in Figure 2g: (1) spectral weight from the lower energy shoulder of the peak at 530 eV is reduced (Fig 2g, inset), (2) spectral weight increases at the 530 eV peak apex and its higher energy shoulder, and (3) a new peak appears around 540 eV. The low-energy shoulder at the 530 eV peak is associated with e_g states (see spin diagram Figure 1), whereas the peak and high-energy shoulder are associated with t_{2g} states. Therefore, this trend indicates a gradual transition to a LS configuration as x increases[13]. Such a trend is confirmed by the Co-L edge, where an overall increase in L_3 and L_2 (Figure 2h, inset) and a decrease in the L_3/L_2 ratio with composition x is also indicative of a systematically more t_{2g} character. These results are consistent with the transport measurements indicating that the transition occurs at higher temperature with increasing x.

While features (1) and (2) support some qualitative conclusions from transport, feature (3) observed at 540 eV in Figure 2g points to different aspects of the electronic structure, as it appears away from the valence band and in the region of Co 4*sp* hybridization with O 2*p*. As the fraction x increases, spectral weight at this energy increases until $x = 0.40$, in which case a clear peak is resolved. This peak that grows larger as x is increased to 0.80. The deep-energy states due to Co 4*sp* hybridization are not studied exhaustively in the literature, but for rare-earth perovskites with transition metals, there does not usually exist an additional peak in this region [27]. However, in this region, additional peaks have been observed in the case of $LaCoO_3$ doped with Sr[28], and in the case of $LaCrO_3$ at below room temperature temperatures[29]. In each case, the new peak is correlated with significant structural distortions, either due to Sr doping, or due to antiferromagnetic ordering at low temperature ($LaCrO_3$). Therefore, these prior observations suggest that the peak observed in our data is indicative of atomic range structural distortions that are strong enough to affect hybridization of Co 4*sp* with O 2*p*. This argument makes sense in light of the large cation disorder and site-to-site variance at the atomic scale, and points to the unique electronic structure found in CCO systems.

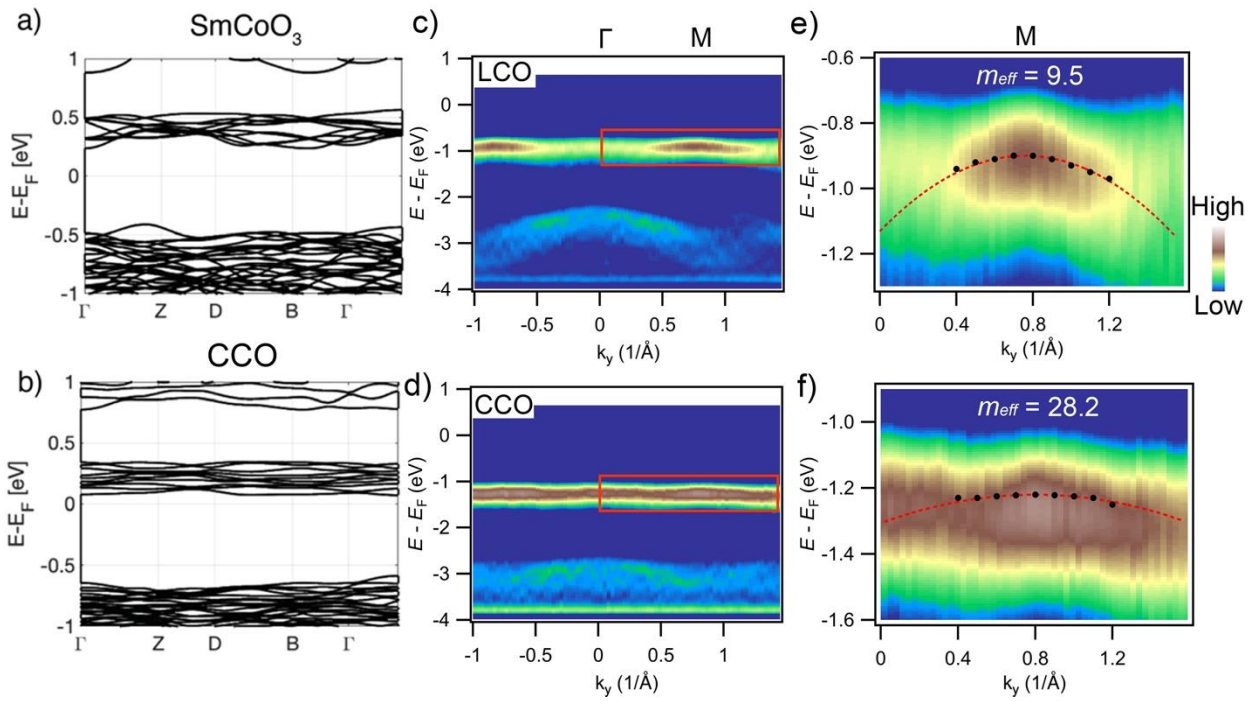

Figure 3. DFT and ARPES data of simple and configurationally complex cobaltate band structure. (a) DFT calculations of band structure for the simple cobaltate $SmCoO_3$ and (b) $(La,Nd,Sm,Gd,Y)_{0.2}CoO_3$ (CCO). (c) 2D curvature ARPES maps for $LaCoO_3$ (LCO) and (d) CCO along Γ – M direction. (e) Its narrowed energy and momentum scales of LCO and (f) CCO (red boxes in Figure 3c,d).

To interpret the experimental observations, we calculate the electronic properties of several simple rare earth cobaltates as well as the CCO ($x = 0.8$) using density functional theory (DFT) within the SCAN+U implementation in conjunction with PAW pseudo-potentials. Previous DFT studies[30, 31] of $LaCoO_3$ found that above 90 K, an equal mixture of high spin (HS) and low spin (LS) Co ions is slightly favored over intermediate spin (IS) configurations. Therefore, for all structures considered, we assume a ratio HS/LS=1, with each LS Co^{3+} surrounded by a HS Co^{3+}, and that the HS ions aligned antiferromagnetically. Figure 3 compares the electronic band structure of $SmCoO_3$ and for CCO at $x = 0.8$, which should be similar from a simple alloying perspective considering

the Goldschmidt tolerance factor. The projected density of states (PDOS) is included in the supplementary text. We present results for spin-up states, as we find insignificant difference between majority and minority spins. Both simple and compositionally complex materials have a similar electronic band gap with 0.65 eV for $SmCoO_3$ and 0.61 eV for CCO with $x = 0.8$. However, while the Fermi level is situated in the middle of the band in $SmCoO_3$ (Figure 3a), it significantly shifts towards the conduction band minimum (CBM) in $x = 0.8$ (Figure 3b). This observation is explained by the fact that in $x = 0.8$, rare-earth disordering leads to an increased effective mass for the electronic states impacted by such disorder. This argument can be justified qualitatively by comparing the flatness of the valence bands in Figure 3a to that in Figure 3b. The shift of the Fermi level towards the CBM indicates that the states near the valence band maximum (VBM) are more impacted than those near the CBM. Indeed, as the PDOS indicates (Figure S3), the states near the VBM have more contribution from rare earths. Moreover, the states in the valence band exhibit more O-Co hybridization than states in the conduction bands as quantified the peak-to-peak ratio between the PDOS for Co and the PDOS for O. For example, for $SmCoO_3$ this ratio is 5.7 for the conduction band versus 1.7 for the valence band, and for the CCO $x = 0.80$ it is 4.8 for the conduction band versus 1.6 for the valence band. Thus, the rare-earth disruption of the O octahedra surrounding the Co ions is expected to impact the valence states disproportionately. As the band structure plots also indicate, the VBM effective mass is indeed significantly smaller in $SmCoO_3$ than in $x = 0.8$. The shift in Fermi level towards the CBM explains the experimentally observed shift from p-type to n-type conduction with increasing compositional complexity.

To validate the outcomes of these calculations, we conduct angle-resolved photoemission spectroscopy (ARPES) measurements on LCO and CCO ($x = 0.8$) at an ambient temperature of around 90 K using a p-polarized light source. We note that, to the best of our knowledge, ARPES

data have not been previously reported for LCO or for any CCO material. We report the first experimentally determined band structures of LCO and CCO x = 0.8, which confirms the mechanism of majority carrier crossover. The 2D curvature ARPES maps of LCO and CCO collected along the Γ – M direction are depicted in Figs. 3c and 3d, respectively[32]. The pristine ARPES maps and constant energy maps are illustrated in supplementary Figure S5. The VBMs of LCO and CCO are situated around -0.71 eV and -0.95 eV below the Fermi level, indicating that LCO and CCO are both insulators at 90 K. To analyze the dispersiveness of the hole pockets at the M point of LCO and CCO, we plot the same data maps with smaller momentum and energy ranges (red boxes in Figure 3c and 3d) in Figure 3e and 3f. The black dots represent bands trajectory via Gaussian fitting of energy dispersion curves (EDC) (supplementary Figure S6). To quantify the dispersiveness of each band, we fit the EDC peaks with a quadratic function (red dashed lines). The effective mass of CCO is approximately three times higher than that of LCO. From measurements of effective mass, we can then calculate the mobility with the measured Seebeck coefficient which is 4.56×10^{-2} and 3.15×10^{-5} cm^2 / V s for x = 0.00 and x = 0.80, respectively (see supplementary Table S1). Therefore, the electronic structures, as revealed by ARPES measurements of LCO and CCO, provide a direct confirmation of our predictions from DFT regarding changes in effective mass.

DISCUSSION

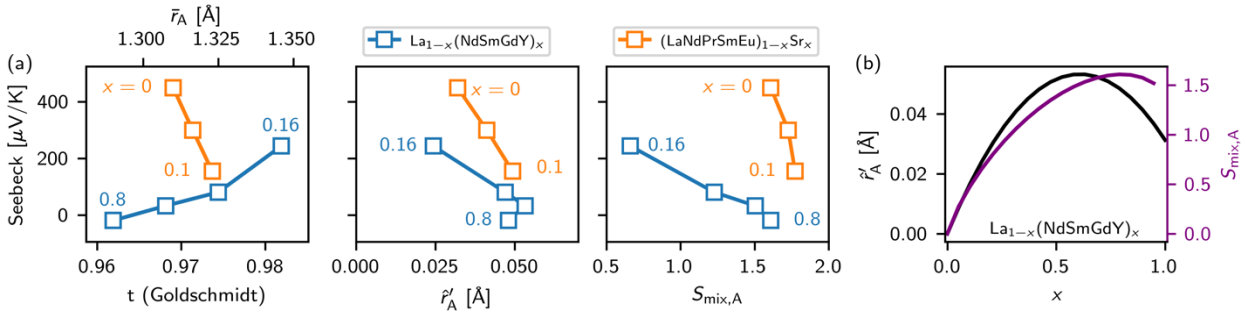

Figure 4. Material descriptors for compositionally complex cobaltates. (a) Seebeck vs. Goldschmidt factor *t* (left panel), $\hat{r}'_A$ (middle panel) and $S_{\mathrm{mix,A}}$(right panel). (b) Comparison of $\hat{r}'_A$ and $S_{\mathrm{mix,A}}$ as a function of x for our composition series.

Our observed p-type to n-type crossover was compositionally induced by A-site alloying alone (i.e., a synthesis strategy not involving either substantial oxygen off-stoichiometry as with $LaCo_{0.2}Fe_{0.8}O_{3-\delta}$ [33], or electron doping as with Ce^{4+} in $LaCoO_3$[34]), and is thus unique in perovskite oxides, to the best of our knowledge. This raises the question: does our compositional series uniquely produce this result, or is it a more general but hitherto unexplored phenomena achievable in other oxide perovskites (cobaltate, nickelate, or other)? We hypothesize the latter. To address this question, we generate material descriptors, including the Goldschmidt factor and plot them in Figure 4. Figure 4a demonstrates how the Goldschmidt factor does not predict transport behavior in high-entropy perovskites and how new predictors are required. As shown in Figure 4a (left panel), for the different alloying strategies between our composition series and that of ref. [21], increasing configurational entropy (increasing x) decreases the Seebeck coefficient but *oppositely* changes the composition-weighted A-site radius $\bar{r}_A$ and therefore the Goldschmidt factor. However, we can derive a more relevant compositional descriptor intended to correlate with structural distortion arising from A-site entropy, given no B-site variation. A simple descriptor that captures the composition-weighted average deviation in A-site radii is $\hat{r}_A = \sum_{i \in A} x_i |r_i - \bar{r}_A|$, but

this equation could nominally be applied to any chemical formula. Instead, we derive a variation that accounts for the octahedral (6-coordinate) arrangement of the A-site network in perovskites to calculate the expected deviation in radii between a central A site and its A-site neighbors. Assuming no short range ordering (i.e., a random A-site solid solution), let c to be one possible 6-coordinate environment (e.g., c = [La, Sm, La, Gd, La, Y], $|c| = 6$), $\mathcal{C}$ be the set of all possible c, and $\pi_c = \Pi_{i \in A} x_i$ be the probability of observing c. We can now write the expected deviation in radii between a central A site and its A-site neighbors as,

$$\hat{r}'_A = \sum_{i \in A} x_i \left(\sum_{c \in \mathcal{C}} \pi_c \sum_{j \in c} \frac{|r_j - r_i|}{|c|} \right).$$

As shown in Figure 4a (center panel), we recover a simple, negatively sloped linear dependence of the Seebeck coefficient as a function of $\hat{r}'_A$ for each composition series. This descriptor qualitatively shares the functional form of an ideal entropy of mixing term, e.g., $S_{\text{mix,A}} = -\sum_{i \in \text{A}} x_i \ln(x_i)$ which therefore also correlates with Seebeck coefficient (Figure 4b). But $\hat{r}'_A$ is a "chemistry-aware" descriptor and can be further tuned by, for example, employing alternative elemental properties to ionic radii (elemental specific volumes, Pauling electronegativity, etc. [35]). These correlations corroborate our previous results that local strain induced by large deviation at the A site may be necessary (although not necessarily sufficient) criteria for carrier type crossover. For example, doping fraction due to substitutions may be the most direct descriptor of carrier type in oxide semiconductors in many cases. However, we anticipate our descriptor will find utility in cases where variance induced localization plays an outsized role, such as the CCO rare earth cobaltates, where the doping fraction alone would not yield our observed experimental trend. In another example, these correlations suggest that $(LaNdPrSmEu)_{1-x}Sr_x$ may also achieve crossover with the maximal mixing entropy composition (x = 0.167). A variety of additional

material systems, for example, $La_{1-x}(NdSmGdY)_x$ with $x > 0.8$, $(LaNdSmGd)_{1-x}Y_x$ with $x \in [0,1]$, and $(LaNdPrSmEu)_{1-x}Sr_x$ with $x > 0.1$, must therefore be characterized to understand or confirm the generality of this trend. Other types of CCOs with two cation sites, such as Ruddlesden-Popper type oxides, may or may not benefit from our proposed descriptor. Studies of these additional systems would shine light on whether compositional descriptors alone, or their combination into simple ML-derived design rules [36], can reasonably predict complex properties (e.g., Seebeck coefficient) more generally in high entropy systems.

CONCLUSION

In conclusion, we have demonstrated that compositional complexity can be used to control properties in rare-earth cobaltates, with several intriguing and surprising functionalities revealed. Tunable rare earth complexity can be used to (1) improve crystallinity at surprisingly low populations of additional rare-earth cations, (2) systematically tune the spin transition threshold, and (3) act as a new method to dope semiconductors. Our structural and XAS analyses suggest that novel electronic properties arise, in part, due to disorder-induced atomic range distortions that force rehybridization of Co 4*sp* states with O 2*p*. The first measurements of ARPES in CCOs were presented alongside DFT calculations of band structure. Together, they reveal new insights into CCO electronic structure, and indicate that the doping mechanism of tunable complexity is asymmetric localization of holes over electrons. Tunable complexity (outside of simple doping/alloying) represents an entirely new way to tune the carrier type and could be relevant to other materials such as nitrides, sulfides, carbides, organic semiconductors, or in any system where atomic-site compositional disorder can asymmetrically affect valence and conduction bands. In particular, these methods may be relevant to compounds that would benefit from improved

crystallinity or phase purity due to entropy stabilization effects. A survey of our results and other works suggest that new material descriptors are needed for property prediction in CCO. We generate a new "chemistry-aware" descriptor for carrier type in high-entropy perovskites and propose that the development of such descriptors will enable the guided discovery of materials with new functionalities and improvements over their compositionally simple counterparts.

METHODS

Raman Spectroscopy

Raman spectra were taken in a Renishaw inVia Raman Microscope using a 532nm laser. Temperature dependence Raman Spectroscopy was done in conjunction with an Instec heater stage with its temperature calibrated by Pt bar evaporated on $LaAlO_3$ substrate.

Electronic transport measurements

Electrical transport measurements were performed in the 4-wire configuration with sputtered Cr/Pt electrodes in a Thermolyne 48000 furnace. A Keithley 6221 current source provided an AC current and SR830 Lock-in Amplifier measured the voltage drop across the inner electrodes. Data were recorded using NHMFL Data Acquisition System v.2.4.1. The temperature was ramped at a rate of 5 K per minute.

Seebeck Measurements

Seebeck measurements were acquired by measuring the thermoelectrical voltage across sets of patterned platinum electrodes. A temperature gradient was set by two Peltier heating and cooling platforms. The thermal gradients between electrodes was measured using an infrared thermal camera FLIR SC6700.

Pulsed Laser Deposition

Epitaxial thin films were grown in a Neocera PLD system on $LaAlO_3$ substrates to a typical thickness of 68 nm, the 266 nm Nd:YAG laser was operated at 5 Hz. The as received LAO substrates were etched in dilute HCl for 30 seconds and rinsed with distilled water, and then annealed in air at 950 °C for 2 hours. $LaCoO_3$ and $La_{1-x}(Nd, Sm, Gd, Y)_{x/4}CoO_3$ ($x = 0.80$) targets were purchased from Toshima Manufacturing Co., Ltd.. During growth, the substrate temperature was 650 °C with O_2 partial pressure of 100 mTorr. The PLD chamber pressure was increased to 2.5 Torr during cooldown. For $x = 0.00$ and $x = 0.80$, only the respective targets are required and duty cycling between the two targets were required for the intermediate x growths by varying the ratio between the number of shots on each target.

X-ray absorption spectroscopy

The XAS spectra were taken at the Advanced Light Source Beamline 7.3.1. Details of the beamline instrumentation and data acquisition are given in ref[37]. Samples were secured on a copper chuck using silver paint, and subsequently loaded into the experimental chamber. Measurements were obtained at a chamber pressure of $2x10^{-8}$ Bar. The incoming X-ray flux was monitored by measuring the drain current from a gold mesh upstream of the experimental chamber. The sample drain current and X-ray fluorescence intensity were measured as a function of X-ray energy (normal incidence) and used to construct the TEY XAS and Total Fluorescence Yield (TFY) XAS respectively. The energy resolution was estimated to be 0.64 eV at the Co L-edge and 0.21 eV at the O K-edge.

Angle-Resolved Photoemission Spectroscopy Measurements.

All ARPES measurements were performed using Scienta R4000 electron analyzer at the base pressure of ~3×10^{-11} Torr in a micro- ARPES end-station at the MAESTRO facility at beamline 7.0.2 at the Advanced Light Source, Lawrence Berkeley National Laboratory. The lateral size of the synchrotron beam was estimated to be between 30 and 50 μm. After transferal of the LCO and CCO films through air to the UHV chamber of APRES, the samples were annealed to 450 °C for 10 minutes for three times with O_2 partial pressure of 5×10^{-5} Torr in the *in situ* PLD chamber. The clean surfaces of the samples were confirmed with *in situ* RHEED after annealing (Supplementary Figure 2). The angular resolution and total energy were better than 0.1° and 20 meV, respectively. We used photon energy of 160 eV to map the energy maps of LCO and CCO for the Γ plane. All experiments were carried out the temperature at 90 K. To facilitate measurements and reduce artifacts from charging, all ARPES samples were grown with a 7 nm metallic underlayer of $La_{0.7}Sr_{0.3}CoO_3$.

ACKNOWLEDGMENTS

This work was supported as part of the Center for Reconfigurable Electronic Materials Inspired by Nonlinear Neuron Dynamics (reMIND), an Energy Frontier Research Center funded by the US Department of Energy (DOE), Office of Science, Basic Energy Sciences. This paper describes objective technical results and analyses. Any subjective views or opinions that might be expressed in the paper do not necessarily represent the views of the US DOE or the United States Government. A.Z., S.O., T.B, C.S., J.D.S, A.C.S., J.Z. M.D.W., S.K, A.A.T. and E.J.F were additionally supported by the Sandia Laboratory-Directed Research and Development (LDRD) Program. Sandia National Laboratories is a multimission laboratory managed and operated by National Technology and Engineering Solutions of Sandia, LLC., a wholly owned subsidiary of Honeywell International, Inc., for the US Department of Energy's National Nuclear Security

Administration under contract DE-NA-0003525. The views expressed in the article do not necessarily represent the views of the US Department of Energy or the United States Government. This research used resources of the Advanced Light Source, which is a DOE Office of Science User Facility under contract no. DE-AC02-05CH11231.

CONFLICT OF INTEREST

The authors declare no conflict of interest.

REFERENCES

[1] B. Jiang *et al.*, "High-entropy-stabilized chalcogenides with high thermoelectric performance," *Science,* vol. 371, no. 6531, pp. 830-834, Feb 19 2021, doi: 10.1126/science.abe1292.

[2] Y. Sun and S. Dai, "High-entropy materials for catalysis: A new frontier," *Sci Adv,* vol. 7, no. 20, May 2021, doi: 10.1126/sciadv.abg1600.

[3] J. L. Braun *et al.*, "Charge-Induced Disorder Controls the Thermal Conductivity of Entropy-Stabilized Oxides," *Advanced Materials,* vol. 30, no. 51, p. e1805004, Dec 2018, doi: 10.1002/adma.201805004.

[4] C. Oses, C. Toher, and S. Curtarolo, "High-entropy ceramics," *Nature Reviews Materials,* vol. 5, no. 4, pp. 295-309, 2020, doi: 10.1038/s41578-019-0170-8.

[5] M. Ahn *et al.*, "Memristors Based on (Zr, Hf, Nb, Ta, Mo, W) High-Entropy Oxides," *Advanced Electronic Materials,* vol. 7, no. 5, 2021, doi: 10.1002/aelm.202001258.

[6] B. Yang *et al.*, "High-entropy enhanced capacitive energy storage," *Nature Materials,* vol. 21, no. 9, pp. 1074-1080, 2022, doi: 10.1038/s41563-022-01274-6.

[7] T. X. Nguyen, Y. C. Liao, C. C. Lin, Y. H. Su, and J. M. Ting, "Advanced High Entropy Perovskite Oxide Electrocatalyst for Oxygen Evolution Reaction," *Advanced Functional Materials,* vol. 31, no. 27, 2021, doi: 10.1002/adfm.202101632.

[8] S. S. Aamlid, M. Oudah, J. Rottler, and A. M. Hallas, "Understanding the Role of Entropy in High Entropy Oxides," *J Am Chem Soc,* vol. 145, no. 11, pp. 5991-6006, Mar 22 2023, doi: 10.1021/jacs.2c11608.

[9] M. Brahlek *et al.*, "What is in a name: Defining “high entropy” oxides," *APL Materials,* vol. 10, no. 11, 2022, doi: 10.1063/5.0122727.

[10] P. B. Meisenheimer *et al.*, "Magnetic frustration control through tunable stereochemically driven disorder in entropy-stabilized oxides," *Physical Review Materials,* vol. 3, no. 10, 2019, doi: 10.1103/PhysRevMaterials.3.104420.

[11] A. R. Mazza *et al.*, "Designing Magnetism in High Entropy Oxides," *Adv Sci (Weinh),* vol. 9, no. 10, p. e2200391, Apr 2022, doi: 10.1002/advs.202200391.

[12] A. R. Mazza *et al.*, "Variance induced decoupling of spin, lattice, and charge ordering in perovskite nickelates," *Physical Review Research,* vol. 5, no. 1, 2023, doi: 10.1103/PhysRevResearch.5.013008.

[13] M. W. Haverkort *et al.*, "Spin state transition in LaCoO3 studied using soft x-ray absorption spectroscopy and magnetic circular dichroism," *Phys Rev Lett,* vol. 97, no. 17, p. 176405, Oct 27 2006, doi: 10.1103/PhysRevLett.97.176405.
[14] S. Yamaguchi, Y. Okimoto, and Y. Tokura, "Bandwidth dependence of insulator-metal transitions in perovskite cobalt oxides," *Phys Rev B Condens Matter,* vol. 54, no. 16, pp. R11022-R11025, Oct 15 1996, doi: 10.1103/physrevb.54.r11022.
[15] Y.-C. Luo *et al.*, "Correlated Oxide Selector for Cross-Point Embedded Non-Volatile Memory," *IEEE Transactions on Electron Devices,* vol. 71, no. 1, pp. 916-921, 2024, doi: 10.1109/ted.2023.3338184.
[16] S. M. Bohaichuk, M. M. Pelella, Y. Sun, Z. Zhang, S. Ramanathan, and E. Pop, "VO2 Switch for Electrostatic Discharge Protection," *IEEE Electron Device Letters,* vol. 41, no. 2, pp. 292-295, 2020, doi: 10.1109/led.2019.2963046.
[17] P. KuanChang, W. Weisong, S. Eunsung, K. Freeman, and G. Subramanyam, "Vanadium Oxide Thin-Film Variable Resistor-Based RF Switches," *IEEE Transactions on Electron Devices,* vol. 62, no. 9, pp. 2959-2965, 2015, doi: 10.1109/ted.2015.2451993.
[18] S. Catalano, M. Gibert, J. Fowlie, J. Iniguez, J. M. Triscone, and J. Kreisel, "Rare-earth nickelates RNiO(3): thin films and heterostructures," *Rep Prog Phys,* vol. 81, no. 4, p. 046501, Apr 2018, doi: 10.1088/1361-6633/aaa37a.
[19] Y. Q. Jia, "Crystal radii and effective ionic radii of the rare earth ions," *Journal of Solid State Chemistry,* vol. 95, no. 1, pp. 184-187, 1991, doi: 10.1016/0022-4596(91)90388-x.
[20] B. Scherrer *et al.*, "Correlation between electrical properties and thermodynamic stability ofACoO3−δperovskites (A=La, Pr, Nd, Sm, Gd)," *Physical Review B,* vol. 84, no. 8, 2011, doi: 10.1103/PhysRevB.84.085113.
[21] A. Kumar, D. Dragoe, D. Berardan, and N. Dragoe, "Thermoelectric properties of high-entropy rare-earth cobaltates," *Journal of Materiomics,* vol. 9, no. 1, pp. 191-196, 2023, doi: 10.1016/j.jmat.2022.08.001.
[22] P. A. Krawczyk *et al.*, "High-Entropy Perovskites as Multifunctional Metal Oxide Semiconductors: Synthesis and Characterization of (Gd(0.2)Nd(0.2)La(0.2)Sm(0.2)Y(0.2))CoO(3)," *ACS Appl Electron Mater,* vol. 2, no. 10, pp. 3211-3220, Oct 27 2020, doi: 10.1021/acsaelm.0c00559.
[23] R. Witte *et al.*, "Magnetic properties of rare-earth and transition metal based perovskite type high entropy oxides," *Journal of Applied Physics,* vol. 127, no. 18, 2020, doi: 10.1063/5.0004125.
[24] Y. Wen and Y. Liu, "Quantitative analysis of atomic-scale local lattice distortions in high-entropy fluorite oxide (Zr0·2Ce0.2Hf0.2Y0·2Al0.2)O2-δ," *Ceramics International,* vol. 49, no. 15, pp. 26141-26146, 2023, doi: 10.1016/j.ceramint.2023.05.081.
[25] L. Martín-Carrón, A. de Andrés, M. J. Martínez-Lope, M. T. Casais, and J. A. Alonso, "Raman phonons as a probe of disorder, fluctuations, and local structure in doped and undoped orthorhombic and rhombohedral manganites," *Physical Review B,* vol. 66, no. 17, 2002, doi: 10.1103/PhysRevB.66.174303.
[26] A. Ishikawa, J. Nohara, and S. Sugai, "Raman study of the orbital-phonon coupling in LaCoO3," *Phys Rev Lett,* vol. 93, no. 13, p. 136401, Sep 24 2004, doi: 10.1103/PhysRevLett.93.136401.
[27] F. Frati, M. Hunault, and F. M. F. de Groot, "Oxygen K-edge X-ray Absorption Spectra," *Chem Rev,* vol. 120, no. 9, pp. 4056-4110, May 13 2020, doi: 10.1021/acs.chemrev.9b00439.
[28] D. D. Sarma *et al.*, "Investigation of hole-doped insulating La1-xSrxCrO3 by soft-x-ray absorption spectroscopy," *Phys Rev B Condens Matter,* vol. 53, no. 20, pp. 13369-13373, May 15 1996, doi: 10.1103/physrevb.53.13369.
[29] K. H. L. Zhang *et al.*, "Hole-induced insulator-to-metal transition inLa1−xSrxCrO3epitaxial films," *Physical Review B,* vol. 91, no. 15, 2015, doi: 10.1103/PhysRevB.91.155129.

[30] A. M. Ritzmann, M. Pavone, A. B. Muñoz-García, J. A. Keith, and E. A. Carter, "Ab initio DFT+U analysis of oxygen transport in LaCoO3: the effect of Co3+ magnetic states," *J. Mater. Chem. A,* vol. 2, no. 21, pp. 8060-8074, 2014, doi: 10.1039/c4ta00801d.

[31] K. Knížek, Z. Jirák, J. Hejtmánek, P. Novák, and W. Ku, "GGA+Ucalculations of correlated spin excitations inLaCoO3," *Physical Review B,* vol. 79, no. 1, 2009, doi: 10.1103/PhysRevB.79.014430.

[32] P. Zhang, P. Richard, T. Qian, Y. M. Xu, X. Dai, and H. Ding, "A precise method for visualizing dispersive features in image plots," *Rev Sci Instrum,* vol. 82, no. 4, p. 043712, Apr 2011, doi: 10.1063/1.3585113.

[33] L. W. Tai, M. M. Nasrallah, and H. U. Anderson, "Thermochemical Stability, Electrical Conductivity, and Seebeck Coefficient of Sr-Doped LaCo0.2Fe0.8O3-δ," *Journal of Solid State Chemistry,* vol. 118, no. 1, pp. 117-124, 1995, doi: 10.1006/jssc.1995.1319.

[34] S. Hébert *et al.*, "Thermoelectric properties of perovskites: Sign change of the Seebeck coefficient and high temperature properties," *Progress in Solid State Chemistry,* vol. 35, no. 2-4, pp. 457-467, 2007, doi: 10.1016/j.progsolidstchem.2007.01.027.

[35] L. Ward *et al.*, "Matminer: An open source toolkit for materials data mining," *Computational Materials Science,* vol. 152, pp. 60-69, 2018, doi: 10.1016/j.commatsci.2018.05.018.

[36] C. J. Bartel *et al.*, "New tolerance factor to predict the stability of perovskite oxides and halides," *Sci Adv,* vol. 5, no. 2, p. eaav0693, Feb 2019, doi: 10.1126/sciadv.aav0693.

[37] F. Yang *et al.*, "In-situ/operando X-ray absorption spectroscopy for energy science at beamline 7.3. 1 of the ALS," *JSSRR,* vol. 34, pp. 306-314, 2021.

TABLE OF CONTENTS

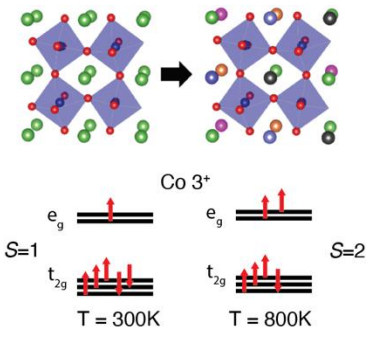

Compositionally complex oxides have shown recent promise as electronic materials, but the role of complexity is often difficult to disentangle from other effects. This paper utilizes compositional complexity as a tunable parameter in an oxide semiconductor to reveal several intriguing functionalities: (1) systematic improvements to crystal quality (2) control over a spin transition, and (3) as a method to dope semiconductors.